JOURNAL OF MATERIALS SCIENCE 23 (1988) 1514–1520

Scanning and high-resolution Auger analysis of zirconolite/perovskite surfaces following hydrothermal treatment

S. MYHRA
School of Science, Griffith University, Nathan, Queensland 4111, Australia
P. DELOGU, R. GIORGI
Dipartimento Tecnologie Innovative Di Base, Divisione Scienza Dei Materiali, ENEA – C.R.E. Casaccia, 00060 Roma, Italy
J. C. RIVIERE
Materials Development Division, UKAERE, Harwell, Didcot, Oxon., UK

Two titanate minerals, zirconolite with perovskite minor phase inclusions, have been subjected to hydrothermal chemical attack. The effects of the treatment have been investigated with scanning and high-resolution Auger analysis. The results suggest that both mineral surfaces act as substrates for carbonate precipitation. Dissolution was found to be the main mechanism of attack for perovskite, followed by precipitation from solution and growth of TiO_2 on the perovskite phase regions. There was also precipitation of calcium as fluoride and phosphate, and growth of these crystallites at random locations on the surface of the two-phase ensemble. The zirconolite phase regions were not affected by the hydrothermal treatment, within the resolution of the present experiment.

1. Introduction

Most schemes which have been devised for the ultimate disposal of high-level nuclear wastes (HLW) from commercial reactor fuel cycles, envisage that the radionucleides be incorporated into a solid waste form before deposition into a suitable geological repository [1]. Synroc is the generic term for waste forms based on assemblages of titanate minerals such as perovskite, zirconolite and hollandite [2]. A number of microstructural studies have been carried out in recent years on Synroc waste forms [3, 4] and titanate minerals [5, 6] in order to establish the necessary data base for evaluation of performance, and to aid further development and optimization of these materials. The performance of HLW waste forms is measured against criteria which relate to actual or potential mechanisms which may release HLW to the biosphere over geological time spans. The chemical durability of the waste form is particularly relevant in the context of a potential breach of containment in which case the solid will be subjected to severe hydrothermal attack. Titanate ceramics are known to be particularly durable when exposed to an aqueous solution at high temperature and pressure [7]. This has been established by standard leach testing procedures and solution analysis [8]. However, detailed surface analytical and electron optical studies have also been carried out, on perovskite in particular [9, 10].

Recent studies of the effect of hydrothermal attack by distilled deionized waters on monolithic and ion-beam thinned TEM foil perovskite specimens [11] have established that this titanate dissolves congruently, probably by way of base catalysed hydrolysis. Solution analysis can be used to monitor the resultant concentration of calcium in solution, while the very low solubilities of titanium compounds preclude this species being readily detectable by such analysis. Rather it is found that TiO_2 will precipitate and grow epitaxially on the dissolving substrates as discrete crystals of anatase or brookite [11]. The temperature above which nucleation and growth occur appears to be approximately 120° C; below this temperature such crystallites cannot be observed even by high-resolution transmission electron microscopy. However, even though dissolution of perovskite, saturation of titanium compounds in solution and precipitation and growth of TiO_2 have been established for the titanate perovskite, several questions remain unanswered.

For instance, the possibility that dissolution is preceded by selective leaching, by ion exchange of H_3O^+ for Ca^{2+}, cannot be ruled out conclusively on the basis of previous work. Secondly, there is some evidence [11, 12] that perovskite is the preferred substrate for precipitation of TiO_2 and that particular orientations are preferred. Moreover, previous work has focused on single-phase perovskite in solution, and a multiphase substrate might exhibit different growth characteristics. Thirdly, it is known, mainly from solution analysis work, that zirconolite is much more resistant than perovskite to hydrothermal aqueous attack. Detailed surface analytical work might provide some insight into the extent and reasons for the durability.

The present work has the following aims. Firstly, it

0022–2461/88 $03.00 + .12 © *1988 Chapman and Hall Ltd.*

seeks to clarify further the relative importance of selective leaching with respect to congruent dissolution of perovskite. Secondly, it extends the investigation to another titanate, namely zirconolite. Finally, it seeks to provide further insight into the merits of the applying surface analytical techniques (Auger electron spectroscopy, AES, and scanning Auger microscopy, SAM, in particular) to processes which are operative at the solid–solution interface.

2. Experimental details

The specimens were fabricated and supplied by the Synroc Research Group in the Australian Nuclear Science and Technology Organisation (ANSTO) at Lucas Heights, Sydney, Australia. Small pellets were produced from calcined precursor powder by cold pressing and sintering in a reducing atmosphere at 1200° C so as to arrive at a material with a large grain size. This procedure makes for ease of microstructural analysis but results conversely in a great deal of open porosity. The zirconolite ($CaZrTi_2O_7$) specimens were analysed by SEM and TEM and found to have a 20% by volume admixture of perovskite ($CaTiO_3$) as a minor phase in phase regions of dimensions 3 to 10 μm. The presence of $CaTiO_3$ regions in zirconolite is most likely due to perovskite being the precursor phase for the formation of zirconolite and related phases [12]. Analyses by XRD and TEM of the precursor calcined powder have shown perovskite to be present at that stage of the fabrication route.

Two hydrothermal runs were carried out. The first one, R1, subjected a specimen to 4 days at 150° C in distilled and deionized water (DDW) in a teflon-lined Parr hydrothermal vessel. One face of the specimen had been polished to 1 μm diamond paste finish and cleaned before the commencement of the run. No further cleaning was carried out after removal of the specimen. The ratio of the specimen surface area to solution volume was approximately 0.08 cm^{-1}. The second run, R2, subjected a similar specimen to 10 days at 250° C in DDW in a sealed gold bag. (The use of teflon is limited to temperatures below 200° C.) The specimen and the DDW were enclosed by a thin gold bag with welded seams. This package was then inserted into a large stainless steel autoclave. The gold bag developed a slow leak during the run and some of the leachant escaped. Thus it is possible to quote only an approximate value for the ratio of surface area to solution volume (0.2 cm^{-1}).

Two different instruments were used to carry out the AES analyses. For R1, an ESCALAB Mk II instrument was used at the Harwell Laboratory, while for R2 a PHI600 dedicated AES/SAM instrument was used at ENEA C.R.E. Casaccia. The features of these instruments are sufficiently different to make it worthwhile discussing the analysis procedures in some detail.

The ESCALAB instrument and its performance are optimized primarily for X-ray photoelectron spectroscopy (XPS). As an AES/SAM instrument the lateral resolution is limited by the beam diameter of the electron gun (> 0.2 μm) and by the mechanical stability of the manipulator sample mount. During the analysis of the surfaces of zirconolite/perovskite specimens detailed scans were carried out in the $N(E)$ mode (direct pulse counting) over the kinetic energy ranges 100 to 800 (for C, O, Ti, Ca) and 1600 to 1950 eV (for Zr). The electron beam energy was 10 keV and the beam current typically 5 nA, which was a compromise imposed by specimen charging, by the need for high count rates and by the requirement of good lateral resolution. The beam diameter would have been $< 0.5\,\mu$m under these conditions. Data were acquired with 0.5 and 1.0 eV energy increments below 800 and above 1600 eV, respectively, at a scan rate of 50 msec per increment and a constant retard ratio (CRR) of 4. Each recorded scan was the averaged sum of ten repetitions. The surface was profiled by ion-beam etching using a static defocused beam (2 keV Ar^+ ions) and a current density of 10 $\mu A\,cm^{-2}$ in order to minimize preferential etching and interlayer mixing. From previous experience [13], we estimate that the etch rate corresponded to about 0.1 nm removal of surface material per unit of integrated dose (ΣD) of 1 $\mu A\,min\,cm^{-2}$.

The PHI600 model is purpose-built for high spatial resolution AES/SAM analysis. High-quality secondary electron images were obtained with a 10 keV electron beam and 0.2 nA beam current. Particular surface features were then analysed by locating the beam at a point in the image. Subsequently elemental mapping was carried out by gating over particular spectral peaks and rastering the electron beam. Typical parameters for the maps were as follows. The beam current was increased to 5 to 15 nA in order to achieve realistic count rates without causing excessive surface charging. Spectral data were obtained for scan increments of 1 and 2 eV below and above 1000 eV, respectively. The rate of scanning was 10 msec per increment and repetitive scanning was carried out for periods of 10 to 20 min in order to achieve good signal-to-noise ratios. The beam diameter would have been close to 20 nm for a current of 0.2 nA in order to have the required image resolution, and considerably larger at 5 to 15 nA (probably > 100 nm). The CRR was 4 and data were obtained in the $N(E)*E$ mode. Surface contamination was removed by ion-beam etching to a dose of 35 $\mu A\,min\,cm^{-2}$ (3 keV Ar^+ ions rastered over a $0.3 \times 0.3\,cm^2$ area).

3. Results and discussion

A secondary electron micrograph obtained with ESCALAB II is shown in Fig. 1. This was taken after the chemical attack R1, and after a light ion-beam etch ($\Sigma D = 5$) which served to remove surface contamination. The perovskite minor phase regions are clearly visible (areas of dark contrast and of dimensions 2 to 5 μm).

Point analyses were carried out within the perovskite and zirconolite phase regions for integrated doses of $\Sigma D = 5$, 20, 70 and 220 (i.e. to a depth of about 22 nm). A subset of the resultant data is shown in Fig. 2. The main Auger peaks are indicated. There are distinctive differences between the two phase regions in accord with the two different stoichiometries ($CaTiO_3(20:20:60)$ and $CaZrTi_2O_7(9:9:18:64)$). In addition, more carbon was found on the surface of

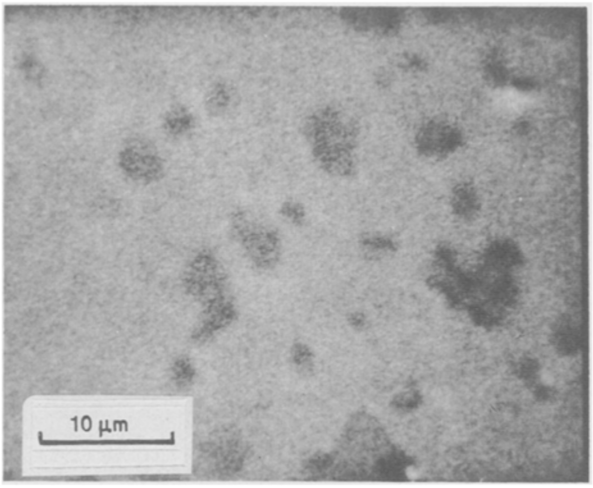

Figure 1 A secondary electron micrograph of zirconolite (grey background) with perovskite minor phase regions (dark areas) after hydrothermal treatment, R1. Surface contamination has been removed by ion-beam sputtering to a dose of 5 μA min cm^{-2}.

perovskite than on zirconolite, probably as a result of the formation of carbonate in accord with previous observations [10]. Also, it is clear from the spectra in Fig. 2 that calcium is depleted in the first few monolayers of the perovskite phase regions. It is unlikely that this species is present as a carbonate rather than as a constituent of perovskite. The changes in the zirconolite spectra are insignificant as functions of sputtering dose.

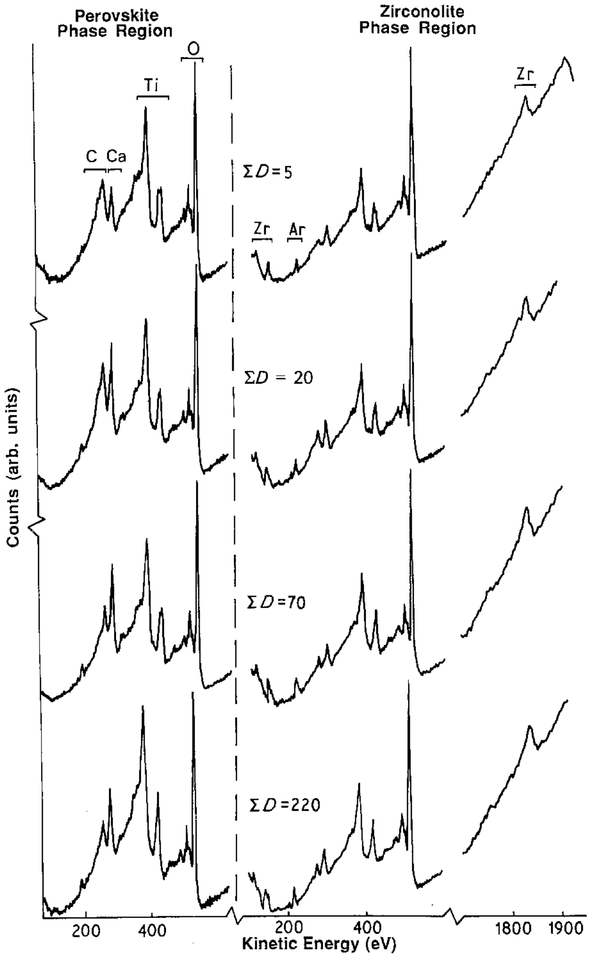

Figure 2 AES data are shown for point analyses within perovskite and zirconolite phase regions as functions of ion-sputtering dose. The main Auger peaks are labelled.

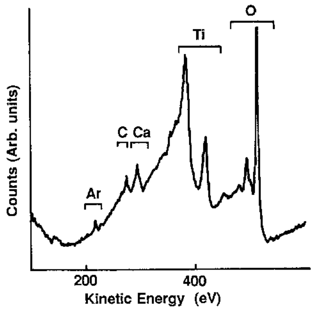

Figure 3 AES data from a point scan within a perovskite phase region after $\Sigma D = 70$. The features exhibited are in accord with the presence of TiO_2 precipitates which are too small to be resolved in the SEM image of Fig. 1.

The point analyses were repeated for many locations within the two phase regions. Those within the zirconolite regions gave results consistently similar within experimental limitations. However, within the perovskite regions considerable differences were observed in spite of the apparently homogeneous appearance (Fig. 1) of the secondary electron image. For instance, Fig. 3 shows a typical point scan, which does not reflect the known stoichiometry of $CaTiO_3$; it should be compared with the scan for perovskite in Fig. 2 after $\Sigma D = 70$. The scan in Fig. 3 shows a spectrum of Ti LMM and O KLL, and little else, while the one in Fig. 2 is substantially in accord with that expected for a perovskite surface.

Kastrissios *et al.* [11], who have used transmission electron microscopy (TEM) to study microstructural features of thin electron-transparent foils of $CaTiO_3$ after hydrothermal attack, have recently shown that perovskite undergoes dissolution with subsequent precipitation and growth of TiO_2 as brookite or anatase on the dissolving substrate. Similar observations have been made by Myhra *et al.* [9], although in a much less direct manner, by investigating surfaces of $CaTiO_3$ after hydrothermal attack with scanning electron microscopy (SEM), XPS and AES. From the work of Kastrissios *et al.*, we expect TiO_2 epitaxial crystallites to have formed on the perovskite substrate. The dimensions of these crystallites would have been too small to be imaged at the resolution available with the ESCALAB II instrument. However, even though these features cannot be imaged, they do manifest themselves during AES analyses (Fig. 3) by placing the analysis point at random locations within the perovskite phase regions. Conversely, there appears to be little, if any, growth of precipitates on the zirconolite phase regions.

Compositional data as functions of ion etching dose (and thus depth below the original surface) were determined by quantification of the spectra. This was carried out by numerical differentiation of the $N(E)$ spectra, application of known elemental sensitivity factors [14] to the peak-to-peak excursions in the differential spectra, and calculating self-consistent compositions. These results are shown in Figs 4a and b for point analyses as functions of dose within the zirconolite and perovskite phase regions, respectively. For $\Sigma D = 70$ and 220 several points were analysed within each phase region. The scatter in the resultant data is

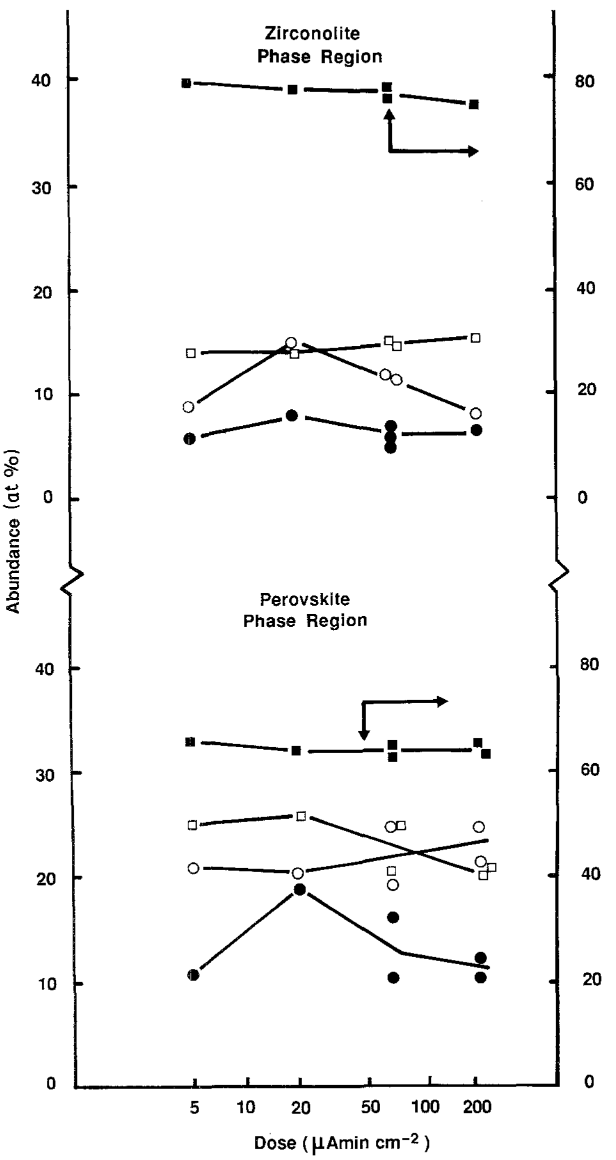

Figure 4 Quantified compositional data (in at % abundance) as functions of ion sputter depth for the perovskite and zirconolite phase regions. The data for the oxygen are scaled to the axis on the right-hand side. (●) Ca, (○) C, (□) Ti and (■) O.

only slight for zirconolite and is representative of experimental uncertainties as well as possible excursions from nominal stoichiometry. The scatter is much greater for the perovskite phase regions, due to the random presence of TiO_2 precipitates. In general the apparent compositions *vis-à-vis* expected stoichiometries show low calcium and titanium and high oxygen. This is due to the fact that average sensitivity factors from the literature [14] were used rather than specific adjusted values. However, the trends as functions of sputtered depth are independent of the choice of sensitivity factors. Also, zirconium was neglected during the quantification procedures because it was measured in a separate scan over a higher kinetic energy region. However, the inferred abundance was invariant, within experimental error, and in rough accord with the expected 9 at % abundance.

The results in Fig. 4 show that there is a near-surface ($\Sigma D = 20$) peak in both the carbon and calcium abundances, in the zirconolite phase regions, suggesting that calcium is present as a carbonate precipitate. In the perovskite phase regions, it is found that carbon and calcium track each other.

Conversely, there is no suggestion of a depleted calcium layer as might be expected if dissolution, rather than selective leaching, of the matrix is the operative mechanism. However, one must be cautious about this interpretation because both TiO_2 and calcium carbonate precipitates might provide partial coverage of the substrate and thus give rise to observations of averaged compositions masking a zone depleted in calcium.

The surface of a similar specimen was examined with the PHI600 AES/SAM after the more severe hydrothermal exposure, R2. Secondary electron micrographs obtained with this instrument are shown in Figs 5a and b. A conventional scanning electron micrograph of a similar surface after similar hydrothermal treatment is shown in Fig. 5c for comparison. The superior imaging of a dedicated high resolution AES/SAM instrument compared with that of the multipurpose XPS/AES/SAM instrument (ESCALAB II) is readily apparent. Image resolution at the submicrometre level is clearly obtainable. The central features exhibiting high contrast due to charging are associated with porosity and are of little interest. The perovskite minor phase regions are well delineated and are found to be etched back from the surface plane of the zirconolite major phase as the result of the hydrothermal treatment. The extent to which this has occurred can be estimated from a high magnification image (Fig. 6). The shadowing in the lower edge of the micrograph is due to the 30° angle of incidence of the electron beam with respect to the "bottom" of the micrograph, from which it can be estimated that the depth is about 0.5 μm. Also, large numbers of columnar and cubic precipitate crystals are found at random locations over both phase regions. Finally, large numbers of streaks of random orientation and bright contrast are visible. The latter features may be due to grain boundaries which may have been decorated by localized selective chemical attack and/or selective nucleation of small precipitate crystallites. Work on perovskite TEM foils [11], mentioned above, suggests that grain boundaries may provide preferred nucleation sites for growth of TiO_2 precipitates.

Point analyses of the surface features described above were carried out with the PHI600 after an ion-beam sputtering dose of 25 μA min cm^{-2} (3 keV Ar^+ ions). Those point analyses obtained from within the "perovskite" regions gave results, without exception, which were consistent with the presence of TiO_2 (Fig. 7a); there were only traces of contaminant carbon and phosphorus. A typical spectrum from a zirconolite phase region is shown in Fig. 7b; the presence of zirconium manifests itself in features at low (100 to 150 eV) and high (1800 to 1850 eV) kinetic energy as the Auger electrons from MNN and LMM excitations, respectively.

Several of the cubic precipitate crystallites were also analysed. A typical spectrum is shown in Fig. 7c. A very large signal from calcium as well as a clearly resolvable F *KLL* feature suggest that this spectrum is representative of CaF_2. Fluorine is an unintentional,

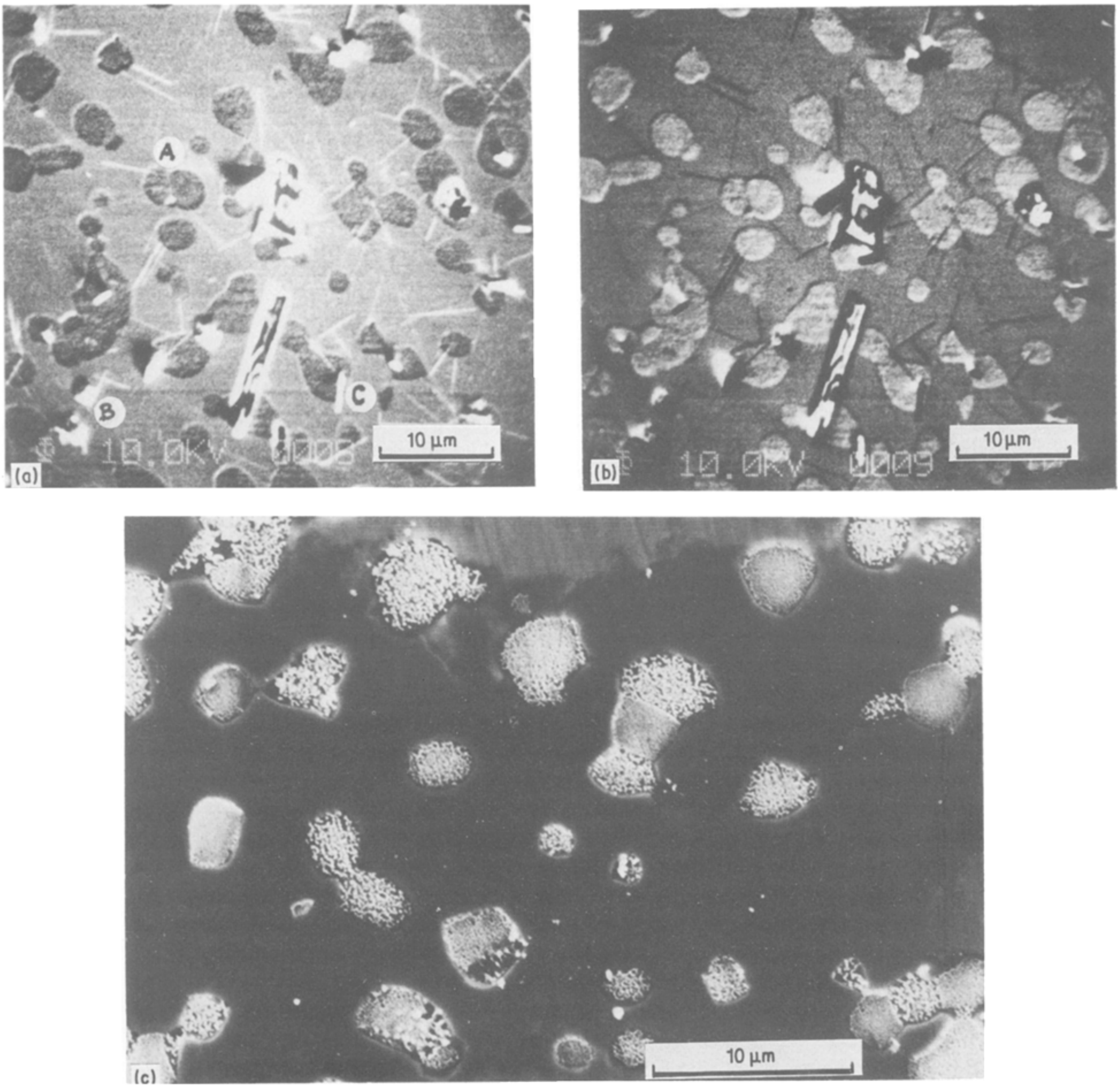

Figure 5 Secondary electron micrographs after treatment, R2, obtained with PHI600 instrument, (a) normal contrast, (b), reverse contrast. The field of view shows porosity (central high contrast features), perovskite phase regions covered in TiO_2 precipitates (A), cubic "CaF_2" precipitates (B) and columnar "$CaPO_4$" precipitates (C). (c) A conventional high-resolution scanning electron micrograph of a similar surface after exposure to comparable hydrothermal conditions.

but not unexpected, contaminant in the system. Likewise, several of the columnar precipitate crystallites were analysed. Typical results are shown in Fig. 7d. The spectrum exhibits a large calcium peak as well as a resolvable contribution from P *LMM* near 110 eV. These columns are, therefore, likely to be $CaPO_4$. Similar observations have been made previously with SEM/EDS [15]. The spectra in Figs 7c and d exhibit relatively small Ti *LMM* peaks at about 380 and 420 eV as well as O *KLL* near 510 eV. These can be ascribed to excitations in the substrate surrounding the small crystallites. Even though the diameter of the primary electron beam was considerably smaller than the smallest dimensions of those crystallites, high-energy electrons were scattered out through the sides of the crystallites and generated Auger electrons from the substrate. This effect is particularly difficult to suppress in the case of the columnar $CaPO_4$ crystals, which grow out from the substrate.

A sequence of SAM images was generated for the field of view shown in Figs 5a and b. The titanium map confirmed the earlier observations and is shown in Fig. 8. The distributions of calcium, zirconium and fluorine were also investigated. The results were not as clear-cut as for titanium, even though the results were in agreement with the point analyses; they are therefore not reproduced.

In summary, one may now make the following observations.

(i) Perovskite is clearly affected by a hydrothermal environment. Under severe hydrothermal conditions in DDW it may be affected to a depth of several micrometres. It is likely that this phase undergoes dissolution, although it is not possible on the basis of present results to rule out conclusively selective extraction of calcium by leaching as a precursor mechanism to that of congruent dissolution.

(ii) Both calcium and titanium enter solution, but are subject to solubility constraints. In the case of calcium we find that it will precipitate as a carbonate

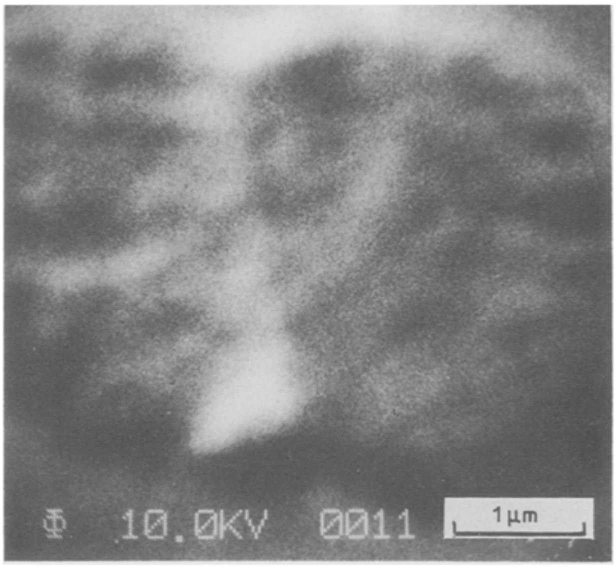

Figure 6 High-magnification view of perovskite phase region (marked A in Fig. 5a) showing shadowing at the lower edge. This is due to the phase region being etched back during hydrothermal exposure.

towards the low end of the hydrothermal temperature range (the presence of carbonate will be affected by the local pH). At more extreme hydrothermal temperatures trace amounts of fluorine and phosphorus will cause the precipitation of calcium as fluoride and phosphate. These precipitates are found randomly over both the perovskite and zirconolite substrates (more correctly one should note that the perovskite phase regions are covered by TiO_2 overgrowths). It is likely that titanium in solution is substantially confined to the double-layer because TiO_2 precipitates are found exclusively on the perovskite substrate. One might expect the double-layer to be bounded laterally by the perovskite phase boundary, thus confining titanium as a species in solution to the double-layer adjacent to the perovskite surface. Conversely, it is possible, but less likely, that titanium may enter solution beyond the double-layer, but that perovskite is the overwhelmingly favoured substrate for epitaxial growth of TiO_2 crystallites.

(iii) Under the range of conditions explored in the present experiment, and subject to the limitations of the surface analytical techniques, zirconolite appears to be substantially unaffected by hydrothermal chemical attack.

(iv) There are some implications of these observations for the use of these two titanates as major mineral phases in the Synroc assemblage. Firstly, zirconolite should perform very well under likely repository conditions. Secondly, because perovskite is subject to an initial dissolution rate in the neighbourhood of $1\,\mu m\,d^{-1}$ in unbuffered DDW for a temperature greater than 200° C, it will be necessary to investigate the reaction paths for strontium in solution; this is the most significant species which has perovskite as its specific destination in the Synroc waste form [2, 12].

Acknowledgements

The present research was funded in parts by the Australian National Energy Research Development and Demonstration Programme, the Harwell

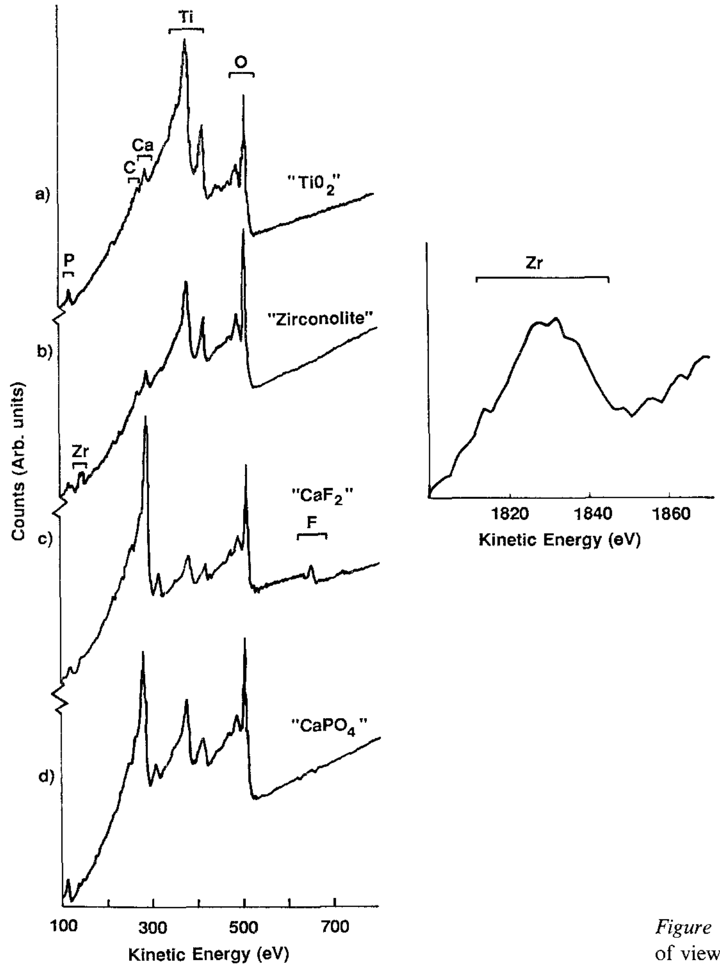

Figure 7 High spatial resolution point analysis from within the field of view of Fig. 5a. The major Auger peaks are identified.

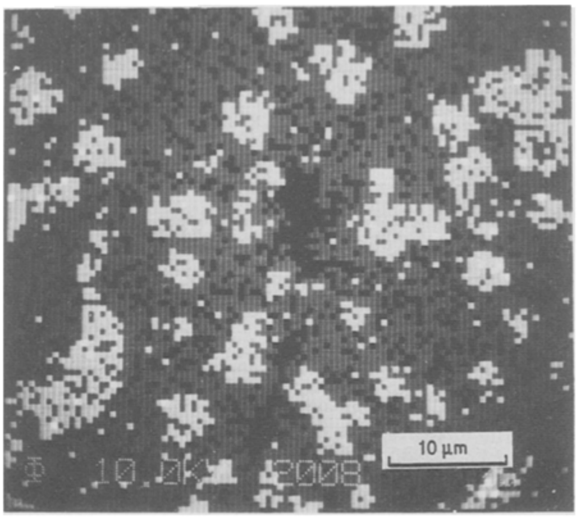

Figure 8 SAM image of titanium distribution over field of view shown in Fig. 5a. Note the good correlation between titanium abundance and the perovskite phase regions (covered with TiO_2 precipitates).

Laboratory Underlying Research Programme, and by ENEA via its grant of access to surface analytical facilities at CRE, Casaccia. One of us (S. Myhra) wishes to acknowledge support and hospitality extended by Harwell and CRE, Casaccia, during periods of attachment to these institutions.

Mr M. Stephenson carried out some of the SEM microscopy, Dr F. Neall provided services during the hydrothermal runs and Dr L. S. Welch assisted during work at Harwell. Finally, specimen materials were supplied by the Australian Nuclear Science and Technology Organization Establishment at Lucas Heights. This work benefited greatly from many useful discussions with the Synroc Research Group at Griffith University, in particular with Mr D. Pham.

References

1. G. J. McCARTHY, *Earth Miner. Sci.* **45** (1975) 17.
2. A. E. RINGWOOD, "Safe Disposal of High Level Nuclear Reactor Wastes: A New Strategy" (ANU, Canberra, Australia, 1978).
3. D. R. COUSENS, S. MYHRA, J. PENROSE, R. L. SEGALL, R. St. C. SMART and P. S. TURNER, in "Scientific Basis for Nuclear Waste Management V", edited by W. Lutze (North Holland, New York, 1982) p. 309.
4. J. A. COOPER, D. R. COUSENS, R. A. LEWIS, S. MYHRA, R. L. SEGALL, R. St. C. SMART, P. S. TURNER and T. J. WHITE, *J. Amer. Ceram. Soc.* **68** (1985) 64.
5. T. J. WHITE, R. L. SEGALL and P. S. TURNER, *Angew. Chem. Int. Ed. Engl.* **24** (1985) 357.
6. S. E. KESSON and T. J. WHITE, *Proc. R. Soc. (London), Ser. A.* **405** (1986) 73.
7. A. E. RINGWOOD, *Mineral Mag.* **49** (1985) 159.
8. A. E. RINGWOOD, V. M. OVERSBY, S. E. KESSON, W. SINCLAIR, N. WARE, W. HIBBERSON and A. MAJOR, *Nucl. Chem. Waste Manag.* **2** (1981) 287.
9. S. MYHRA, H. E. BISHOP, J. C. RIVIERE and M. STEPHENSON, *J. Mater. Sci.* **22** (1987) 3217.
10. S. MYHRA, D. SAVAGE, A. ATKINSON and J. C. RIVIERE, *Amer. Mineral.* **69** (1984) 902.
11. T. KASTRISSIOS, P. S. TURNER and T. J. WHITE, *J. Amer. Ceram. Soc.* **70** (1987) c-144.
12. P. E. FIELDING and T. J. WHITE, *J. Mater. Res.* **2** (1987) 387.
13. S. MYHRA, H. E. BISHOP and J. C. RIVIERE, *Surf. Technol.* **19** (1983) 145.
14. D. BRIGGS and M. P. SEAH, "Practical Surface Analysis by Auger and X-ray Photoelectron Spectroscopy" (Wiley, New York, 1983).
15. M. STEPHENSON, School of Science, Griffith University, personal communication (1987).

Received 15 July
and accepted 9 October 1987